Void Nucleation, and Growth during Tensile Deformation of Nanoscale Precipitated Steel and Bainitic Steel

Mugita, Yasutaka
Department of Materials Physics and Chemistry, Kyushu University

Aramaki, Masatoshi
Department of Materials Science and Engineering, Kyushu University

Yamamoto, Masayuki
Yamamoto Scientific Tool Lab. Co., Ltd.

Takeuchi, Akihisa
Japan Synchrotron Radiation Research Institute

他

出版情報：ISIJ International. 59 (7), pp.1362-1368, 2019-07-15. 日本鉄鋼協会
バージョン：

ISIJ International, Vol. 59 (2019), No. 7, pp. 1362–1368

Void Nucleation, and Growth during Tensile Deformation of Nanoscale Precipitated Steel and Bainitic Steel

Yasutaka MUGITA,[1)]* Masatoshi ARAMAKI,[2)] Masayuki YAMAMOTO,[3)] Akihisa TAKEUCHI,[4)] Miyuki TAKEUCHI,[5)] Takeshi YOKOTA,[6)] Yoshimasa FUNAKAWA[6)] and Osamu FURUKIMI[2)]

1) Department of Materials Physics and Chemistry, Kyushu University, 744 Motooka, Nishi-ku, Fukuoka, 819-0395 Japan.
2) Department of Materials Science and Engineering, Kyushu University, 744 Motooka, Nishi-ku, Fukuoka, 819-0395 Japan.
3) Yamamoto Scientific Tool Lab. Co., Ltd., 2-15-4 Sakae-cho, Funabashi, Chiba, 273-0018 Japan.
4) Japan Synchrotron Radiation Research Institute, 1-1-1 Kouto, Sayo-gun, Hyogo, 679-5198 Japan.
5) Department of Graduate School of Agriculture and Life Sciences, The University of Tokyo, 1-1-1 Yayoi, Bunkyou-Ku, Tokyo, 113-8657 Japan.
6) Steel Research Laboratory, JFE Steel Corporation, 1 Kawasaki-cho, Chiba-city, Chiba, 260-0835 Japan.

(*Received on November 21, 2018; accepted on February 5, 2019; J-STAGE Advance published date: March 28, 2019*)

A local elongation of 8% for nanoscale precipitated steel was observed via tensile testing, which is higher than that of 5% for bainitic steel. To determine the factor underlying this difference, void nucleation, growth, and coalescence mechanisms in the nanoscale precipitated steel and the bainitic steel were examined using electron backscattering diffraction and subsequent observation by synchrotron radiation X-ray laminography during tensile testing. Synchrotron radiation X-ray laminography analysis of void growth and coalescence revealed that the critical strain and the critical void volume fraction for fracture in the bainitic steel were smaller than those for the nanoscale precipitated steel. Secondary-ion mass spectrometry analyses revealed that C atoms were segregated at grain boundaries in the bainitic steel. Void nucleation sites in the nanoscale precipitated steel were nanoscale precipitates inside the grain and at grain boundaries and coarse precipitates; however, in the bainitic steel, void nucleation sites were entirely at grain boundaries. Nanoindentation hardness measurements showed a larger plastic strain gradient between the grain boundary and matrix in the bainitic steel than in the nanoscale precipitated steel. From these results, the high local elongation exhibited by the nanoscale precipitated steel was concluded to be due to the reduced plastic strain gradient with a uniform hardness distribution between the grain boundary and the grain interior.

KEY WORDS: synchrotron radiation x-ray; 3D image analysis; high-tensile-strength steel; strain concentration.

1. Introduction

To achieve reductions in the weight of vehicles, the automotive industry requires the development of high-strength steel with high-formability. Therefore, many types of high-strength steels have been developed in order to meet this requirement, where the most common type is nanoscale precipitated steel.[1)] This steel is particularly characterized by its higher hole expansion ratio, λ,[1)] compared with that of other high tensile strength steels, such as bainitic steel, martensitic steel, dual-phase (DP) steel,[2)] and transformation-induced plasticity (TRIP)-assisted steel.[3,4)] However, the mechanism underlying the high λ value in the nanoscale precipitated steel is still not clear; elucidating this mechanism is expected to further improve λ values and allow the development of a new type of high-strength steel.

Generally, λ is evaluated using a hole expansion test,[5)] which has been shown to have a linear relationship to a local elongation obtained from tensile testing.[6)] In the hole expansion test, a piercing process is performed before the hole expansion. Voids nucleate in this piercing process. On the other hand, in the local elongation region of tensile testing, void nucleation and growth accompanies increasing stress triaxiality.[7,8)] These voids eventually coalesce, resulting in fracture.[9–11)] These phenomena mean that the local elongation depends on the process of void nucleation, growth, and coalescence; here, "void growth" refers to an increase in the volume of an individual void and does not include the coalescence of multiple voids. Therefore, the study of void nucleation, growth, and coalescence during tensile testing is important to develop the high-strength steel with the high λ value.

In our research group, the processes of void nucleation, growth, and coalescence were previously studied using synchrotron radiation X-ray laminography,[12–14)] and we revealed that the high local elongation is caused by the suppression of sudden void growth near the fracture caused by

* Corresponding author: E-mail: mugita@zaiko15.zaiko.kyushu-u.ac.jp
DOI: https://doi.org/10.2355/isijinternational.ISIJINT-2018-762

a low strain concentration at the grain boundary.[15,16)]

In this study, cyclic loading–unloading tensile testing was performed by applying sequential changes in strain until near final fracture for both nanoscale precipitated steel and bainitic steel. Void nucleation and growth were investigated by synchrotron radiation X-ray laminography, which enables the three-dimensional (3D) observation of voids in flat tensile test specimens. The void nucleation sites in the fractured specimens were also observed using electron backscattering diffraction (EBSD). In addition, the factor controlling the local elongation is discussed based on the differences in hardness between the grain boundaries and interiors as measured by nanoindentation hardness testing.

2. Experimental

2.1. Test Specimens

In this study, the nanoscale precipitated steel and the bainitic steel were used, both with a tensile strength of 780 MPa. The nanoscale precipitated steel was recently developed to increase λ.[1)] The λ values of the nanoscale precipitated steel and bainitic steel used in this study were 100% and 75%, respectively. The bainitic steel was conventional high-tensile steel. The specimens were prepared by hot rolling process. The finishing temperature and coiling temperature were held at 1 173 K and 723 K, respectively.

The chemical compositions are shown in **Table 1**. The tensile test specimens had a width and thickness of 2.0 and 1.2 mm, respectively, the parallel section was 3.0 mm long. These dimensions were chosen to fit the synchrotron radiation X-ray system used to observe the voids (see section 2.3).

The microstructures of both steels were observed by using a field emission scanning electron microscope (FE-SEM; Ultra 55, Carl Zeiss AG, Germany) for planes perpendicular to the rolling direction (RD) at an accelerating voltage of 15 kV. The test specimens were embedded in resin and polished with emery papers, followed by polishing to a mirror finish with alumina buffing. The specimens were then etched with a 3 vol.% nitric acid–97% ethanol solution. The coarse precipitates in both steels were observed by using optical microscope (OM) for planes perpendicular to the RD. The surface was polished with emery papers, followed by sequential polishing with α-alumina and colloidal silica solutions.

The microstructures and misorientations in grain of both steels were observed by using EBSD. The inverse pole figure (IPF), kernel average misorientation (KAM) and misorientations in grain were analyzed using Orientation Imaging Microscopy analysis software (OIM™; AMETEK Co., Ltd., USA).

Thin foils were prepared from the specimens to observe the nanoscale precipitates in the nanoscale precipitated steel using transmission electron microscopy (TEM; CM20 FEG, Netherlands) at an accelerating voltage of 200 kV. In addition, the precipitates were observed by energy dispersive X-ray spectroscopy (EDS) for the planes perpendicular to the RD at an accelerating voltage of 15 kV.

Table 1. Chemical compositions of steels used in this study (mass%).

Specimen	C	Si	Mn	P	S	Others
Nanoscale precipitated steel	0.05	0.1	1.4	0.01	0.001	Ti, V
Bainitic steel	0.09	0.7	1.5	0.02	0.001	Ti

2.2. Measurement of C in Grain Boundaries

Test specimens of 10 mm in diameter and 1 mm in thickness were prepared from both steels for secondary ion mass spectrometry (SIMS) analysis. The plane perpendicular to the normal direction (ND) was used for SIMS analysis. The sample surfaces were polished with emery papers, followed by sequential polishing with α-alumina and colloidal silica solutions to prepare the samples for elemental mapping by SIMS (Nano SIMS 50L, CAMECA, USA). Using a 16 keV Cs^+ primary ion beam, $12C^-$ was detected with an incident beam current of 1.0–1.5 pA and dwell time of 10 ms/px at 15×15 μm^2 over an area of 256×256 px^2.

2.3. Void Observation by Synchrotron Radiation X-Ray Laminography

Flat tensile test specimens with the same dimensions used for measuring the strength and the elongation were cut such that the tensile direction was parallel to the RD. After the surfaces of the specimens were polished with 1 200-grit emery paper, cyclical tensile loading–unloading was performed in six stages from immediately after the maximum load point to near fracture at an initial strain rate of 1.0×10^{-3} s^{-1}. The tensile tests of the nanoscale precipitated steel were stopped at plastic strain (ε_p) values of 0.07, 0.12, 0.29, 0.56, 0.63, and 0.71 (near final fracture). Similarly, tests using the bainitic steel were stopped at ε_p values of 0.05, 0.12, 0.22, 0.29, 0.38, and 0.48 (near final fracture). Here, ε_p was defined by Eq. (1):

$$\varepsilon_p = \ln\left(\frac{A_0}{A}\right) \quad \text{..... (1)}$$

where A_0 is the initial cross-sectional area of the test specimen, and A is the area of the cross-section when the tensile test was stopped, which was calculated from the thickness and the width of the tested specimen.

Using the test pieces from each of the above-mentioned strain states, 3D images of the voids was collected using X-ray laminography at the BL20XU beamline of SPring-8, a large-scale synchrotron radiation facility.[14)] A variable visible light conversion high-resolution X-ray image unit (BM-AA50 and ORCA-FLASH 4.0 sCMOS camera, Hamamatsu Photonics, Japan) was used as a detector. An X-ray energy of 37.7 keV was chosen. The voxel size was 0.51 μm, and the specimen rotational axis inclination for laminography measurement was 45°. Considering the composition of the specimen and the thickness of the test piece, an adequate transmission intensity was obtained under these conditions. The number of projections for the laminography scans was 3 600/360° and each projection image was acquired with an exposure time of 600 ms.

After median-filter processing (2×2 px) of the projection data obtained by laminography, two-dimensional (2D) cross-sectional images were reconstructed using the filtered back-projection method considering the inclination of the rotational axis. 3D images were reconstructed and analyzed

using the Avizo image analysis program (version 9.1.1; FEI, USA), using 2 048 2D tomographic images as layers.

2.4. Analysis of Void Nucleation Sites by EBSD

After tensile testing to final fracture, test specimens were cut from the failed specimens with a fine cutter to examine void nucleation sites using SEM-EBSD. These test specimens were embedded in resin to observe the plane perpendicular to the transverse direction (TD). The surface was polished with emery papers, followed by sequential polishing with α-alumina and colloidal silica solutions. Secondary electron (SE) images were acquired using FE-SEM, and EBSD images were obtained at an accelerating voltage of 15 kV. The void nucleation sites were then analyzed using OIM™.

2.5. Nanoindentation Hardness Test

The hardness distribution from the grain boundaries to the grain interior was investigated for specimens deformed until the maximum stress. The test specimens were embedded in resin to measure the hardness of the plane perpendicular to TD, and then polished using α-alumina and colloidal silica solutions. The nanoindentation hardness (H_{IT}) was measured with an instrumented indentation tester (ENT-2100, Elionix, Japan). The number of measurement points was 300 (30 lines × 10 columns), and the test force was 9.8 mN. After the hardness measurements, the specimens were etched with a 3 vol.% nitric acid–97% ethanol solution. The closest distance between the grain boundary and the apex of the triangle formed by indentation was measured to investigate the relationship between H_{IT} and the distance from the grain boundary.

3. Results and Discussion

3.1. Microstructures

The microstructures of the nanoscale precipitated steel and the bainitic steel observed by SEM and OM are depicted in **Fig. 1**, where their average grain diameters were 5 μm and 3 μm, as shown in **Figs. 3**(a) and 3(c), respectively. We defined grain boundaries with an orientation difference of 15° or more in this study. Figure 1(b) depicts the microstructure of the bainitic steel used in this study. This steel consisted of 80% upper bainite and 20% lower bainite.

Figures 1(c) and 1(d) show the precipitates observed in both steels, which exhibit rectangular cross-sections. The observed precipitates and analysis results for the nanoscale precipitated steel are shown in **Figs. 2**(a)–2(d). Figures 2(a) and 2(b) show a TEM image and an EDS spectrum, respectively, of the nanoscale precipitates (seen in rows). Titanium, vanadium, and carbon were detected in the nanoscale precipitates, other than iron originating from matrix. Meanwhile, Figs. 2(c) and 2(d) show a SEM image and an EDS spectrum, respectively, of the coarsened TiN precipitates. These results showed that nanoscale carbides and coarse TiN simultaneously precipitated in the

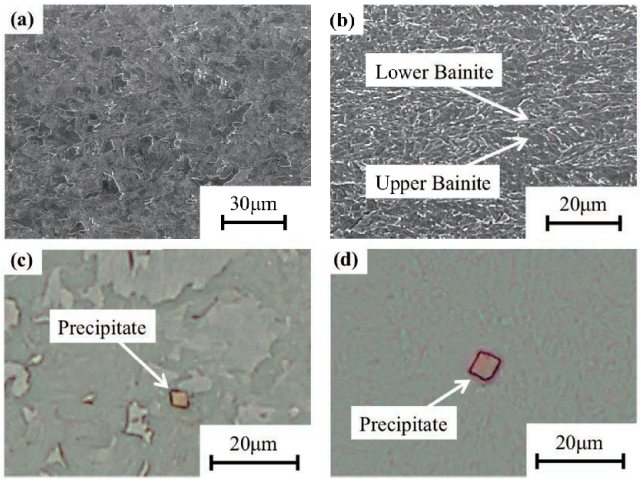

Fig. 1. Micrographs, (a) SE image and (c) OM image for nanoscale precipitated steel, (b) SE image and (d) OM image for bainitic steel. (Online version in color.)

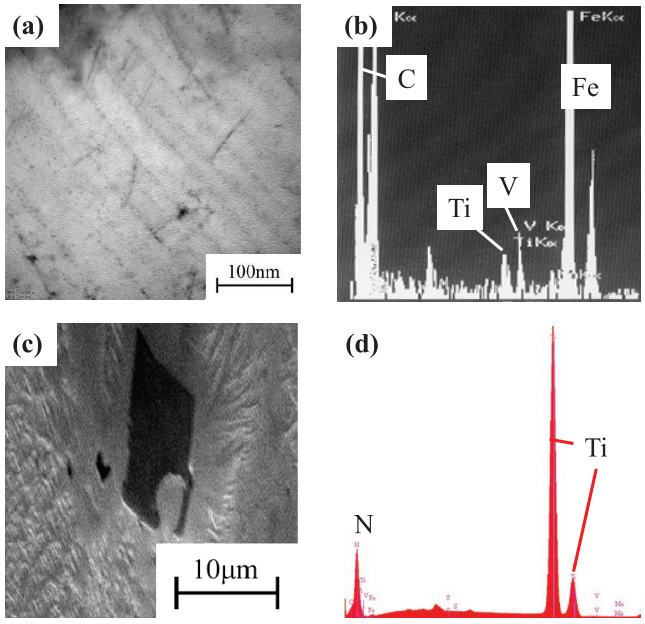

Fig. 2. Precipitates in nanoscale precipitated steel, (a) TEM image and (b) EDS map of nanoscale precipitates, (c) SEM image and (d) EDS map of coarse precipitate. (Online version in color.)

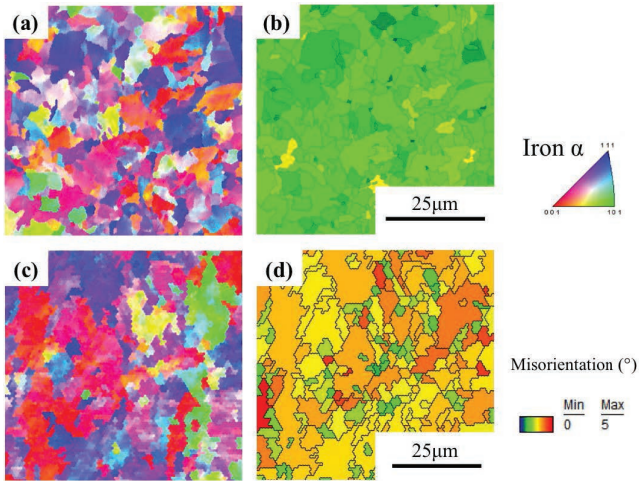

Fig. 3. EBSD analysis results, (a) IPF map (b) grain average misorientation map for nanoscale precipitated steel, (c) IPF map and (d) grain average misorientation map for bainitic steel. (Online version in color.)

nanoscale precipitated steel. The precipitate in the bainitic steel depicted in Fig. 1(d) was concluded to be TiN based on the configuration.

It is known that the local misorientation is correlated with the dislocation density.[17,18] Therefore, Figs. 3(b) and 3(d), which show the misorientation of each grain, indicate that the bainitc steel had a higher dislocation density than the nanoscale precipitated steel. From these results, it was inferred that the dislocation strengthening was strongly influenced in the bainitic steel, while the strengthening by the fine precipitates was dominant in the nanoscale precipitated steel. With the combination of these strengthening mechanisms, both steels had the same strength.

3.2. C in Grain Boundaries

Cs^+-induced SE images of the nanoscale precipitated steel and the bainitic steel are shown in **Figs. 4**(a) and 4(c), respectively, along with SIMS $12C^-$ elemental maps for the nanoscale precipitated steel and the bainitic steel in Figs. 4(b) and 4(d), respectively. The enrichment of atomic C at the grain boundary was clearly observed in the bainitic steel, while not in the nanoscale precipitated steel samples. Since retained austenite was not observed and carbon was discontinuously observed at the grain boundary by SIMS, carbon should be enriched and precipitated as carbide at the grain boundary.

3.3. Tensile Tests and Void Observation

Nominal stress–strain curves obtained from the tensile testing of the nanoscale precipitated steel and the bainitic steel are shown in **Fig. 5** (see **Table 2** for the strength and elongation data). The lower yield point (LYP) and the tensile strength (TS) were almost identical for both steels, although the uniform and local elongations of the nanoscale precipitated steel were higher than those of the bainitic steel. The higher uniform elongation in the nanoscale precipitated steel was expected to enhance recovery during tensile deformation, accompanied by promotion of secondary slips or cross slips on a finer scale due to the nanoscale precipitates.[1] In this study, we focused on the local elongation from the view point of void nucleation, growth, and coalescence as the plastic strain gradient is related to the void nucleation sites. No voids were observed just before the maximum stress point by SEM.

The tested specimens were then observed by X-ray laminography and 3D images were constructed (as shown in **Fig. 6**). In this figure, the voids are colored to distinguish them clearly. At near fracture, the nanoscale precipitated steel clearly showed more voids than the bainitic steel. **Figure 7** shows 3D images of the voids in the nanoscale precipitated steel for ε_p values of 0.12 to 0.29, where it can be seen that new voids nucleated sequentially. This tendency was also observed for the bainitic steel. Changes in the number (N) and volume fraction (V_f) of the voids for each ε_p value obtained during the tensile tests are shown in **Figs. 8**(a) and 8(b). Both N and V_f increased with increasing ε_p for both steels. The changes in N and V_f of voids with ε_p tended to be the same for both steels as shown in Figs. 8(a), 8(b). These results suggest that there is no difference between the both steels for void growth behavior. These results also show that the ε_p value resulting in void coalescence in the nanoscale precipitated steel was higher than that for the bainitic steel, consistent with the larger local elongation of the former.

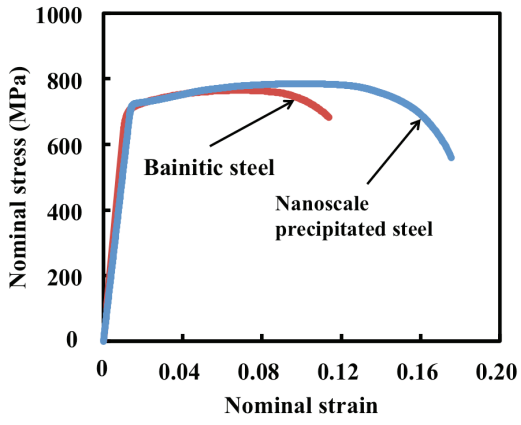

Fig. 5. Nominal stress–strain curves obtained for nanoscale precipitated steel and bainitic steel. (Online version in color.)

3.4. Void Nucleation Sites

After the two steels were tensile tested until final fracture, the void nucleation sites were investigated using inverse pole figure (IPF) maps produced from EBSD data. The IPF map (body-centered cubic: bcc Fe) of the nanoscale precipitated steel revealed that voids nucleated in the grain interior

Table 2. Strength and elongation of steels used in this study.

Specimen	0.2% Proof Strength (MPa)	Tensile Strength (MPa)	Uniform Elongation (%)	Local Elongation (%)
Nanoscale precipitated steel	703	785	9	8
Bainitic steel	696	765	5	5

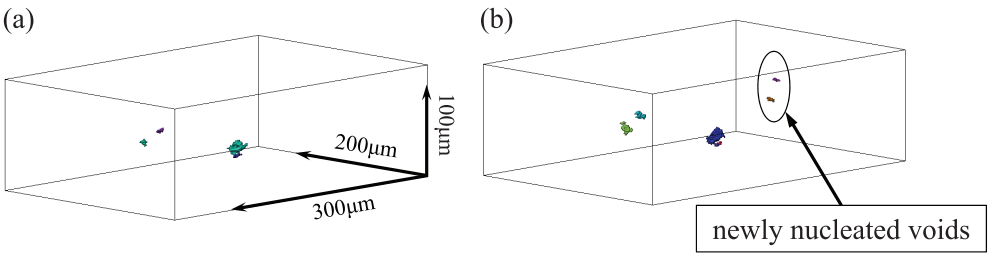

Fig. 7. 3D images of voids obtained by laminography for nanoscale precipitated steel, (a) ε_f = 0.12 and (b) ε_f = 0.29. (Online version in color.)

(**Fig. 9**(a)), at grain boundaries (Fig. 9(b)), and at fragments of coarse TiN precipitates (Fig. 9(c)). Although the point void nucleation at the grain interior was not detected, it was thought to be nanoscale precipitates. The void nucleation sites of the nanoscale precipitated steel were nanoscale precipitates in the grain interior, the grain boundaries (without coarse precipitates), and coarse precipitates (grain interior and grain boundaries). The ratios of nucleation sites in the grain interior, at grain boundaries, and at coarse precipitates were 20%, 30%, and 50%, respectively (averages of ten observations). **Figure 10** shows the IPF map (bcc Fe) of the bainitic steel, where void nucleation was only observed

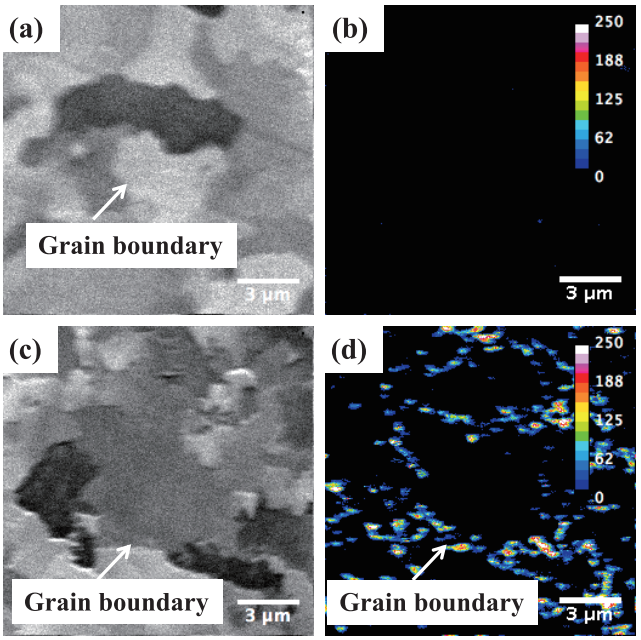

Fig. 4. SIMS analysis results, (a) SE image and (b)12C$^-$ mapping for nanoscale precipitated steel, (c) SE image and (d) 12C$^-$ mapping for bainitic steel.

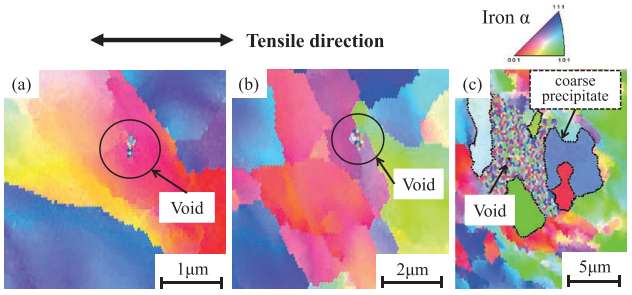

Fig. 9. IPF maps showing void nucleation sites observed after fracture for nanoscale precipitated steel. (a) Inner grain, (b) grain boundary, and (c) coarse precipitate.

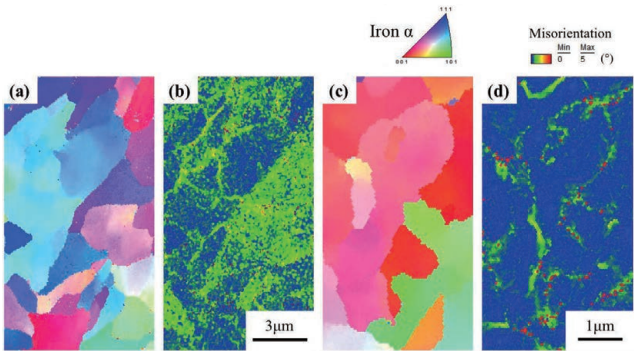

Fig. 12. EBSD analysis results, (a) IPF map (b) KAM map for nanoscale precipitated steel, (c) IPF map and (d) KAM map for bainitic steel.

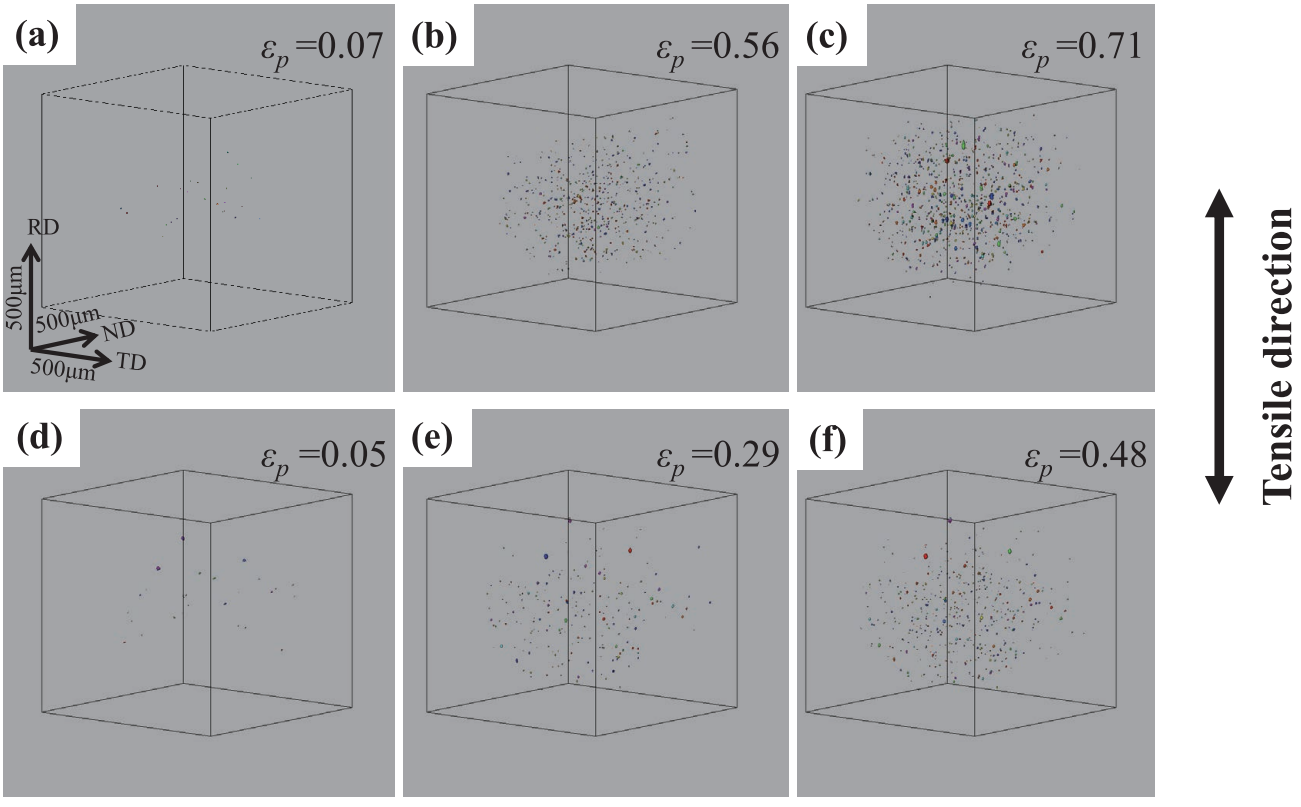

Fig. 6. 3D images of voids obtained by laminography, (a, b, c) Nanoscale precipitated steel, (d, e, f) Bainitic steel.

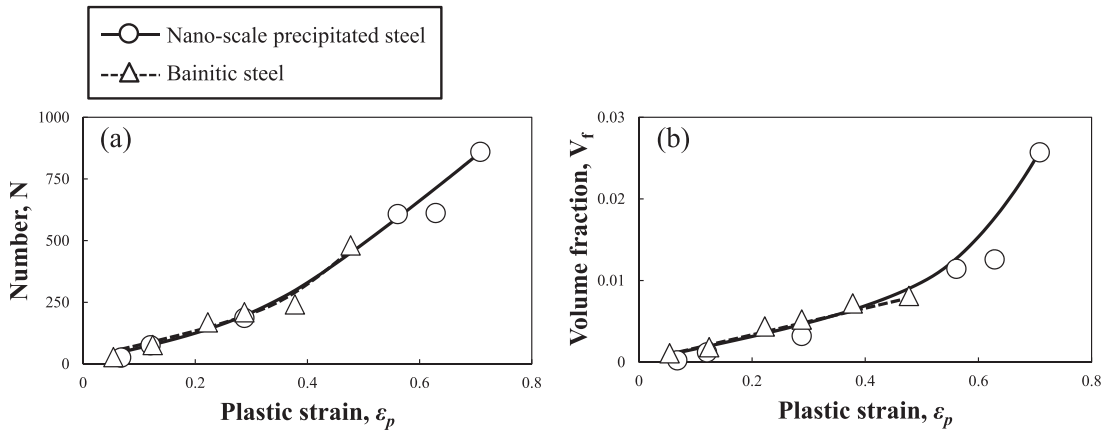

Fig. 8. Changes in the (a) number and (b) volume fraction of voids during plastic strain.

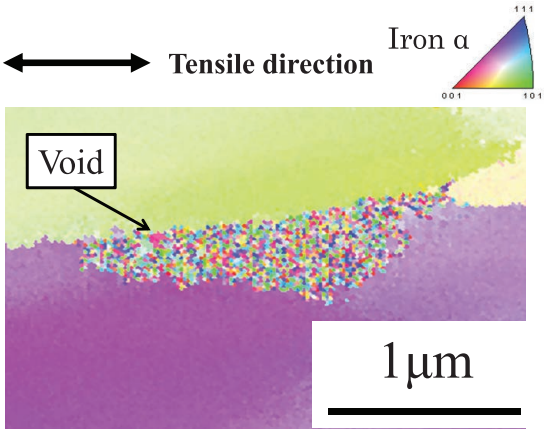

Fig. 10. IPF maps showing void nucleation sites observed after fracture for bainitic steel. (Online version in color.)

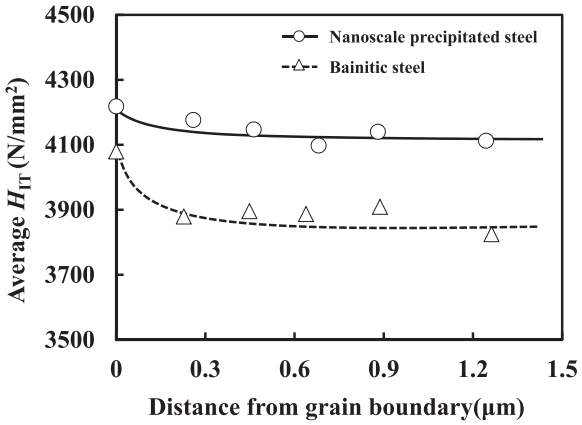

Fig. 11. Average nanoindentation hardness, H_{IT}, as a function of distance from the grain boundary for nanoscale precipitated steel and bainitic steel.

at the grain boundary.

3.5. Nanoindentation Hardness

The relationship between the average H_{IT} and distance from the grain boundary for the two steels measured until the maximum stress during tensile testing is shown in **Fig. 11**. The difference between the average H_{IT} values at the grain boundary and those in the grain interior of the bainitic steel was larger than that of the nanoscale precipitated steel; this was attributed to the distribution of C atoms around the grain boundaries, as shown in Fig. 4(d). These nanoindentation results strongly suggested that the strain concentration around the grain boundaries in the bainitic steel was larger than that in the nanoscale precipitated steel. Furthermore, it is considered that the strain concentration became small because nanoscale carbides were dispersed in the grain in the nanoscale precipitated steel.

KAM maps are shown in **Fig. 12**. The misorientation values around the grain boundaries for the bainitic steel were larger than these for the nanoscale precipitated steel. The misorientation causes the strain concentration, so this result shows the same tendency as the nanoindentation results.

Void nucleation mechanisms are broadly categorized into homogeneous and heterogeneous nucleation; the former mainly involves an increase of the dislocation density and vacancy migration, whereas heterogeneous nucleation occurs at sites containing particles such as inclusions, precipitates, or other discontinuous structures.[19] Grain boundaries are representative discontinuous structures. Homogeneous nucleation of voids is caused by the condensation of lattice vacancies; however, this mechanism cannot occur below ~300 K as the vacancy diffusion rate is extremely low. Therefore, the voids are expected to nucleate at particles such as inclusions, precipitates, or grain boundaries for both steels studied here. In general, voids are generated at areas with larger strain concentrations. The difference between the average H_{IT} at the grain boundaries and in the grain interiors was higher for the nanoscale precipitated steel than that for the bainitic steel, showing that the strain concentration at the grain boundaries of the bainitic steel was higher than that in the nanoscale precipitated steel, consistent with the areas of void formation. So, the local elongation of the nanoscale precipitated steel became larger than that of the bainitic steel for strain concentration at the grain boundaries was suppressed. This result is consistent with our previous studies.[15,16]

4. Conclusions

Void nucleation sites in nanoscale precipitated steel and bainitic steel were examined using IPF maps prepared from EBSD data, while the void growth and coalescence process

was studied using synchrotron radiation X-ray laminography. Furthermore, C atom enrichment at the grain boundaries was observed using SIMS and the hardness distribution near the grain boundaries was measured using nanoindentation tests.

The IPF maps showed that the voids nucleated at the grain interior, grain boundaries, and at fragments of coarse precipitates (TiN) in the nanoscale precipitated steel. Meanwhile, all voids nucleated at the grain boundaries in the bainitic steel. The 3D laminography results revealed that both the number of voids and void volume fraction increased with increasing plastic strain for both steels. Generally, it is thought that large particles form void much easily than small particles. However, in this study the change in the number of voids and volume fraction of voids with ε_p tended to be the same for both steels as shown in Figs. 8(a) and 8(b). This result suggests that there is no difference between the both steels for void growth behavior.

SIMS analysis verified C enrichment at the grain boundaries of the bainitic steel.

We observed that the bainitic steel had a larger difference between hardness values at the grain boundaries and the grain interiors than the nanoscale precipitated steel, attributed to the larger strain concentration at the grain boundaries of the bainitic steel. The local elongation of the nanoscale precipitated steel became larger than that of the bainitic steel for strain concentration at the grain boundaries was suppressed. Based on these findings, we conclude that reducing the strain concentration by forming an alloy with the same hardness at the grain boundaries and grain interiors is an effective method for increasing the local elongation.

Acknowledgements

Funding: This work was partially supported by the Advanced Characterization Nanotechnology Platform of The University of Tokyo, as a part of the Nanotechnology Platform Technology Japan project of the Ministry of Education, Culture, Sports, Science & Technology and the Japan Synchrotron Radiation Research Institute [grant number: 2017B1088].

REFERENCES

1) Y. Funakawa, T. Shiozaki, K. Tomita, T. Yamamoto and E. Maeda: *ISIJ Int.*, **44** (2004), 1945.
2) S. Hayami, T. Furukawa, H. Gondoh and H. Takechi: Formable HSLA and Dual-Phase Steels, ed. by A. D. Davenport, TMS, Warrendale, PA, (1979), 167.
3) V. F. Zackay, E. R. Parker, D. Fahr and R. Busch: *Trans. Am. Soc. Met.*, **60** (1967), 252.
4) T. Nakamura and K. Wasaka: *Tetsu-to-Hagané*, **61** (1975), 2067 (in Japanese).
5) R. Narayanasamy, C. Sathiya Narayanan, P. Padmanabhan and T. Venugopalan: *Int. J. Adv. Manuf. Technol.*, **47** (2010), 365.
6) T. Nakagawa, M. Takita and K. Yoshida: *J. Jpn. Soc. Technol. Plast.*, **11** (1970), 142 (in Japanese).
7) S. Jun: *Eng. Fract. Mech.*, **39** (1991), No. 5, 799.
8) Y. Zhang and Z. Chen: *Int. J. Fract.*, **143** (2007), 105.
9) P. F. Thomason: *J. Inst. Met.*, **96** (1968), 360.
10) J. Kadkhodapour, A. Butz and S. Ziaei Rad: *Acta Mater.*, **59** (2011), 2575.
11) H. Toda, F. Tomizato, R. Harasaki, D. Seo, M. Kobayashi, A. Takeuchi and K. Uesugi: *ISIJ Int.*, **56** (2016), 883.
12) Y. Suzuki, K. Uesugi, N. Takimoto, T. Fukui, K. Aoyama, A. Takeuchi, H. Takano, N. Yagi, T. Mochizuki, S. Goto, K. Takeshita, S. Takahashi, H. Ohashi, Y. Furukawa, T. Ohata, T. Matsushita, Y. Ishizawa, H. Yamazaki, M. Yabashi, T. Tanaka, H. Kitamura and T. Ishikawa: *AIP Conf. Proc.*, **705** (2004), 344.
13) M. Hoshino, K. Uesugi, A. Takeuchi, Y. Suzuki and N. Yagi: *AIP Conf. Proc.*, **1365** (2011), 250.
14) M. Hoshino, K. Uesugi, A. Takeuchi, Y. Suzuki and N. Yagi: *J. Jpn. Soc. Synchrotron Radiat. Res.*, **26** (2013), 257 (in Japanese).
15) O. Furukimi, Y. Takeda, M. Yamamoto, M. Aramaki, S. Munetoh, A. Takeuchi, H. Ide and M. Nakasaki: *Tetsu-to-Hagané*, **103** (2017), 475 (in Japanese).
16) O. Furukimi, S. Harada, Y. Mugita, M. Aramaki, M. Yamamoto, A. Takeuchi, M. Takeuchi and Y. Funakawa: *ISIJ Int.*, **58** (2018), 943.
17) E. Demir, D. Raabe, N. Zaafarani and S. Zaefferer: *Acta Mater.*, **57** (2009), 559.
18) K. Nomura, K. Kubushiro, Y. Sakakibara, S. Takahashi and H. Yoshizawa: *J. Soc. Mater. Sci., Jpn.*, **61** (2012), 371 (in Japanese).
19) B. Dodd and Y. Bai: Ductile Fracture and Ductility, Academic Press, London, (1987), 85.